Tribology International 159 (2021) 106993

Contents lists available at ScienceDirect

Tribology International

journal homepage: http://www.elsevier.com/locate/triboint

Power loss reduction for tilt pad journal bearings utilizing pad pockets and steps

Jongin Yang, Alan Palazzolo *

Department of Mechanical Engineering, Texas A&M University, College Station, TX77840, USA

ARTICLE INFO

Keywords:
Tilting pad journal bearing
Power loss reduction
Journal bearing performance improvement

ABSTRACT

Tilting Pad Journal Bearing (TPJB) are ubiquitous in turbomachinery from small high speed compressors to large turbine generator sets. The TPJB's power losses increase with machine size and speed, reaching as high as 1–2 MW loss (equivalent power for about 1000 homes) per bearing, in a large turbine generator. This study presents a novel power loss reduction technique, inserting a pocket and step in the pads, to activate cavitation in the pocket while maintaining pad stability. The benefits are demonstrated via Thermo-Elasto-Hydrodynamic (TEHD) CFD simulations comparing results with and without these modifications. The novel approach shows power loss reductions up to −27% without a load capacity loss, while reducing required supply oil flow, and peak pad temperature.

1. Introduction

Saving energy has become more and more important due to increased population and global warming issues. In a recent study [1], it was reported that the tribological contact friction consumes around 20% of total global energy, and it was concluded that the greatest potential for reducing CO2 emissions lies in new tribology technologies by 2050, including surface treatments, modification, and texturing on the journal bearing. The ideal bearing has a high lift with low drag like an airplane wing. Many surface texturing studies have been conducted for plain journal bearings over the last several years [2–8]. The technique implants dimples with circular shapes [2–5], rectangular shapes [6–8], etc. on the bearing surface.

The research for reducing power loss has been mainly performed for plain journal bearings through simulations and experiments. In contrast, there is very little parallel research on TPJBs despite their versatility and numerous applications. Starvation is a common power loss reduction way, which is implemented by simply reducing the supply oil flow rate [9]. However, the method reduces load capacity and minimum film thickness between the journal and bearing surface. Also, starvation increases maximum pad temperature and cooling requirements. Ding et al. [10] presented a power loss reduction idea for flooded lubrication TPJB. This reduces the pressure at the supply oil inlet for the bearing and induce air entrainment from the outlet. However, this could destabilize a tilting pad leading to pad fluttering [11,12]. In addition, the over-dissolved air may lead to air contamination issues worsening the lubricant quality. Another approach for bearing loss reduction utilizes directed lubrication, with nozzles and open seals [13] to minimize churning losses near the supply oil inlet. Directed lubrication is already a commercialized and widely used technology. The method presented here can be combined with directed lubrication to obtain further, substantial power loss reductions.

Modeling limitations have played a part in the slow pace for advancing TPJB power loss reduction. Highly accurate TPJB models includes multiphysics capabilities [14,15] required to model Fluid-Structure Interactions (FSI) and Thermo-Elasto Hydrodynamic (TEHD) interactions. Reynolds and CFD models are the major methods to predict bearing performance. The conventional Reynolds approach has limitations for the TPJB simulations due to the over-simplifications of the flow physics (fluid inertia and cavitation) between the journal and modified bearing surface. More accurate TEHD CFD models for TPJB have been presented recently [16–18], and are utilized here to analyze the proposed TPJB performance.

This study provides the theoretical analysis and simulation results for a novel TPJB design to obtaining energy savings, that has the following advantages:

(a) Significant reductions in drag power loss
(b) Maintains load capacity and pad stability
(c) Reduces supply oil flow rate and peak pad temperature
(d) Minimizes changes in dynamic force coefficients

* Corresponding author.
E-mail addresses: jiyang@tamu.edu (J. Yang), a-palazzolo@tamu.edu (A. Palazzolo).

https://doi.org/10.1016/j.triboint.2021.106993
Received 15 January 2021; Received in revised form 22 February 2021; Accepted 10 March 2021
Available online 18 March 2021

Nomenclature

$C_{l,b}$	Radial Bearing Clearance, m
$C_{l,p}$	Pad Clearance, m
h_{tot}	Total enthalpy, J/kg
K_p	Loss coefficient
k	Turbulent kinetic energy, m2/s2
m_{pr}	Preload
R	Radius, m
Re	Reynolds number
r	Volume fraction
p	Pressure, Pa
$p^{'}$	Modified pressure, Pa
p_{cav}	Saturation pressure, Pa
T	Temperature, degC
u	Fluid velocity, m/s
x_s	Total shaft displacement in the x direction (global coordinate), mm
x_{pvt}	Total pivot displacement in the x' direction (local coordinate), mm
y_s	Total shaft displacement in the y direction (global coordinate), mm
λ	Thermal conductivity, J/(m*K)
ρ	Density, kg/m3
δ_{tlt}	Total pad angular displacement (local coordinate), deg
μ	Dynamic viscosity, Pa*s
γ	Turbulent intermittency
ω	Turbulent frequency, 1/s
δ	Mesh displacement, m
σ	Cavitation number
ε	Eccentricity ratio
ω_s	Spin frequency, 1/s
DT	Drag Torque, Nm
PL	Power loss, W

Subscripts

f	Fluid
Eff	Effective
α	liquid or gas (vapor) phases
l	Liquid
V	Vapor
S	Shaft
P	pad
Bb	Bubble

Acronyms

CFD	Computational Fluid Dynamics
FEA	Finite Element Analysis
FSI	Fluid Structure Interaction
RANS	Reynolds Averaged Navier Stokes
TEHD	Thermo-Elasto-Hydrodynamics
TPJB	Tilting Pad Journal Bearing

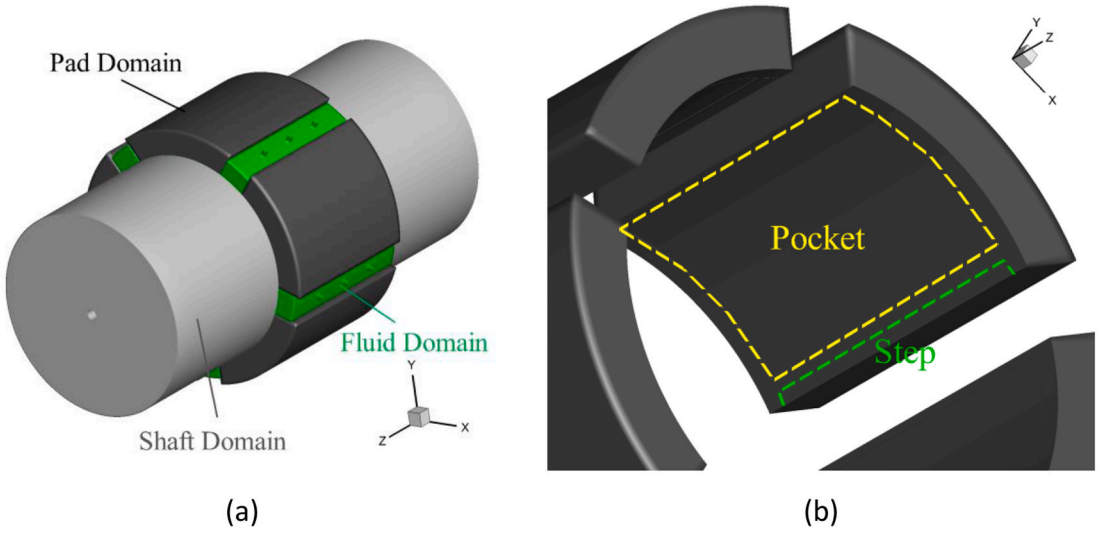

Fig. 1. Schematic of a TPJB System with three nozzles; (a) Overview, (b) Step (green) and Pocket (yellow) included on a Pad. (For interpretation of the references to color in this figure legend, the reader is referred to the Web version of this article.)

The proposed novel modifications to the conventional TPJB is to insert a pocket and step on the unloaded pads, which varies the bearing clearance in the pocket and step regions. The purposes of the pocket and step are (1) generating cavitation inside the pockets to reduce the shear-stress and to (2) stabilize the pads by causing the peak pressure to occur at the pocket and step trailing edges. The phase change from liquid to vapor in the pockets, referred to as cavitation, decreases the shear stress at the journal surface due to the low gas viscosity. The cavitation reduces power loss proportional to the shear stress reduction. The static and dynamic performances of a conventional and the novel TPJB are compared to show the benefits of the novel TPJB. These simulations are performed using a high fidelity TEHD-CFD model to accurately include the pocket and step features.

2. Power loss reduction approach

This section explains the approach to reduce power loss, as validated by TEHD-CFD simulations. The TPJB geometry including all computational domains is depicted in Fig. 1(a). The TPJB shown has five pads, with directed lubrication provided by three nozzles. This arrangement could be generalized for different numbers of pads and nozzles. Direct lubrication lowers power loss significantly, and it is included to show that the proposed TPJB changes can even further reduce power loss. The proposed method is simply to include a pocket and a step in each upper

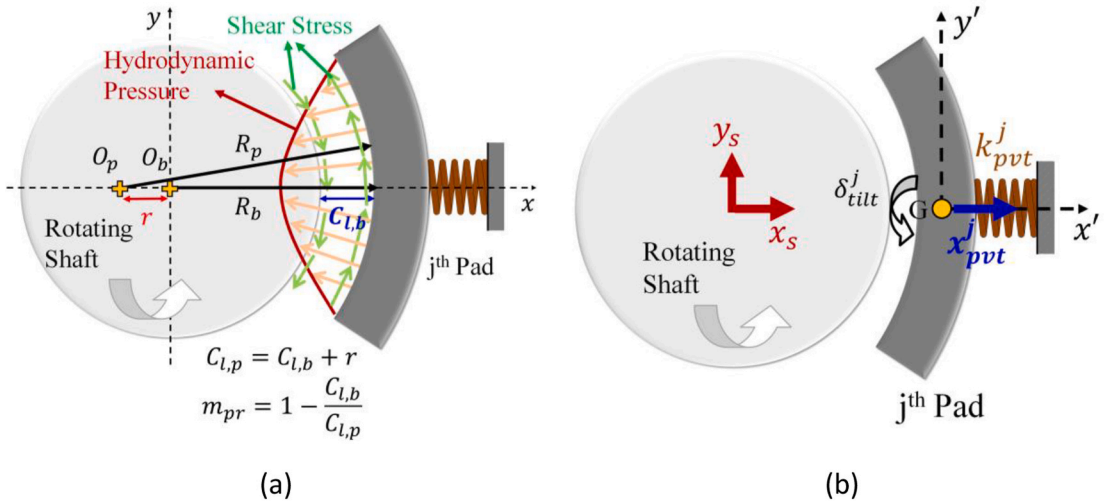

Fig. 2. Journal-Bearing system (a) geometric parameters depicted with hydrodynamic pressure and shear stress, and (b) degrees of freedom.

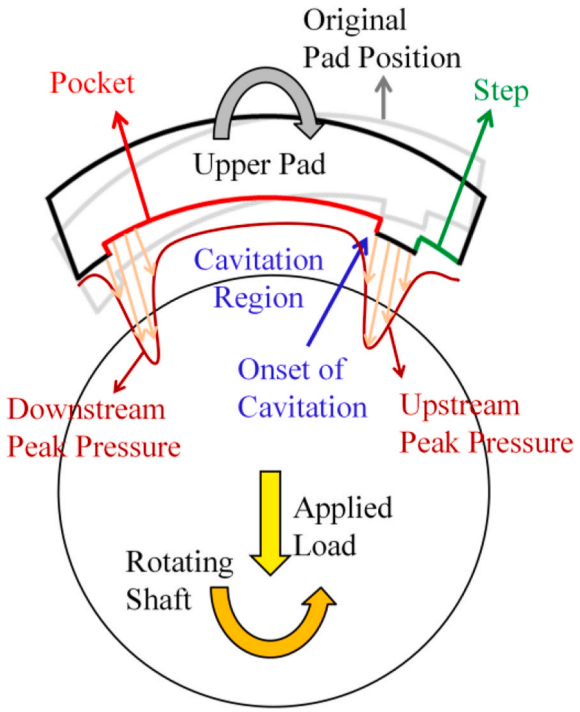

Fig. 3. Cavitation mechanism created by a pocket and a step in the top pad.

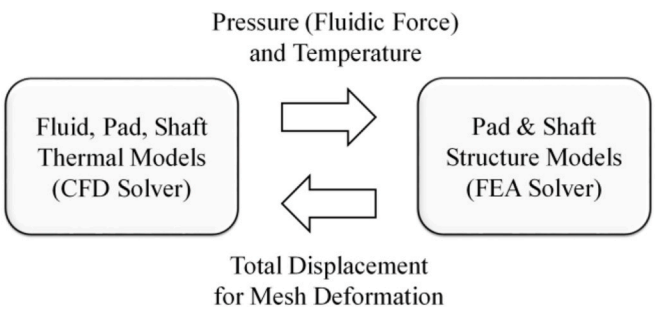

Fig. 4. Fluid structure interaction (FSI) model for a TPJB

pad, as illustrated in Fig. 1(b).

The TPJB is used to support the shaft, and to provide desired stiffness and damping for vibration control. Oil flows from the three nozzles to both side seals and to the thin fluid-film between the journal and the downstream pad. The pressure and shear stress acting on the journal and pad are illustrated in Fig. 2(a). These cause the lifting force and drag force on the shaft, respectively. Important geometric parameters include the bearing clearance ($C_{l,b}$), pad clearance ($C_{l,p}$), and preload (m_{pr}), as shown in Fig. 2(a). The pressure and shear stress induced forces, and the applied loads, determine the equilibrium values of the journal and pad degrees of freedom ($x_s, y_s, \delta^j_{tilt}, x^j_{pvt}$), represented in Fig. 2(b).

Fig. 3 shows a TPJB with a pocket and step designed to lower drag power loss. The pocket and step are inserted in the upper pad, with the step at the leading edge having a much shorter circumferential length than the downstream pocket. The pocket and step have the dual functions of stabilizing the pad motion at an equilibrium tilt angle, and reducing the drag loss by increasing the vapor volume fraction in the cavitation region. Cavitation is the phase change from liquid to gas, and occurs when the pressure becomes lower than the ambient or saturation pressure. The journal drag is significantly reduced if cavitation occurs, since the vapor phase has a much lower effective viscosity. Downstream peak pressure is generated at the pocket's trailing edge so that the pad is rotated in the opposite direction of shaft rotation. Here, cavitation starts to occur slightly downstream of the leading edge of the pocket. The pocket and step are applied in the pads located opposite to the applied load direction. This causes the eccentricity ratio to be reduced, the minimum film thickness increased, and the loading on the "upper" pads to be lower than on the "bottom" pads. The dynamic performance of the bearing, characterized by stiffness and damping, is altered by installing the steps and pockets. This change though is not large, since the primary effects of the steps and pockets is shear stress reduction, while causing only a minor change in load capacity, especially for highly loaded bearings. Pad tilt angle equilibrium position stability is enhanced by the upstream peak pressure being balanced by the downstream peak pressure as illustrated in Fig. 3.

3. TEHD CFD modeling method for a pocketed TPJB

3.1. Overall description

The 3 components that determine the bearing's static and dynamic performance include the journal and adjacent shaft segments, the pads, and the fluid domains. Commercial ANSYS software for CFD (CFX) and FEA (Finite Element Analysis, Mechanical APDL) are utilized to simulate

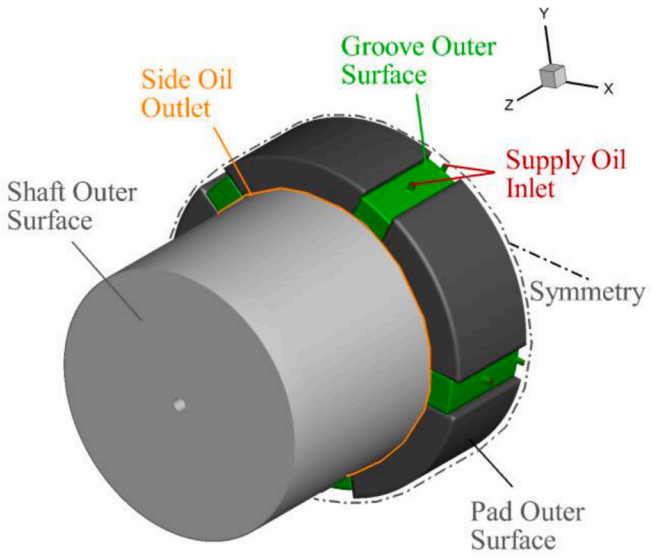

Fig. 5. Prescribed boundary conditions for the CFD solver.

the multiphysics phenomenon (Fluid-Structure Interaction, FSI) of the TPJB system. Fig. 4 shows both solver's inputs and outputs are exchanged through a python-based code (Job Script). The CFD code provides a 3D thermal, transitional turbulence, multiphase flow solution for the fluid domains, along with the heat conduction solution in the pad and shaft domains, including the shaft rotational convection effect. The CFD code's solution for the fluid domain's pressure and the solid domain's temperature are transferred to the solid domains in the FEA solver. The FEA solver then yields displacements caused by centrifugal force on the shaft, and from thermal-elastic deformation of the solid domains. The total displacement solutions from the FEA solver are applied to the boundary faces of the CFD solver, which are the interface boundary between the shaft and fluid domains and between the pad and fluid domains. These total displacements update the interface boundary location values for the mesh deformation equation in the CFD solver. In addition, pad tilting, pad pivot, and shaft translational induced displacements are determined from a Newton-Raphson based equilibrium search algorithm. These displacements are also used to update the

Table 1
Input parameters for smooth and pocketed tilting pad journal bearings.

Parameters	Value
Shaft Diameter [mm]	80
Bearing Length [mm]	60
Bearing Clearance [mm]	0.08
Number of Pads	5
Pad Thickness [mm]	10
Pad Arc Length [degree]	56
Pad Offset	0.5
Applied Load [kN]	5–15
Preload	0.25
Operating Speed [kRPM]	7–13
Pivot Type	Rocker (Cylindrical)
Load Type	Load between pad (LBP)
Outside H.C.C. [W/m^{2}K]	50
Ambient Temperature [C]	30
Supply Total Pressure [kPa]	20–80
Lubricant	ISO 32 [16]
Material (Solid Domains)	Steel

H.C.C: Heat Convection Coefficient

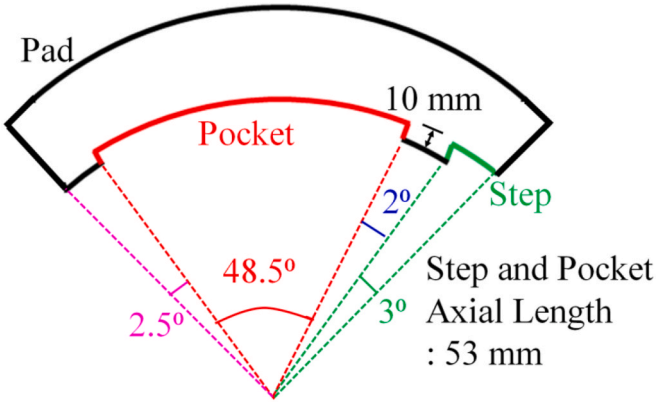

Fig. 7. Pocketed TPJB Pad Dimensions in 3D CFD model.

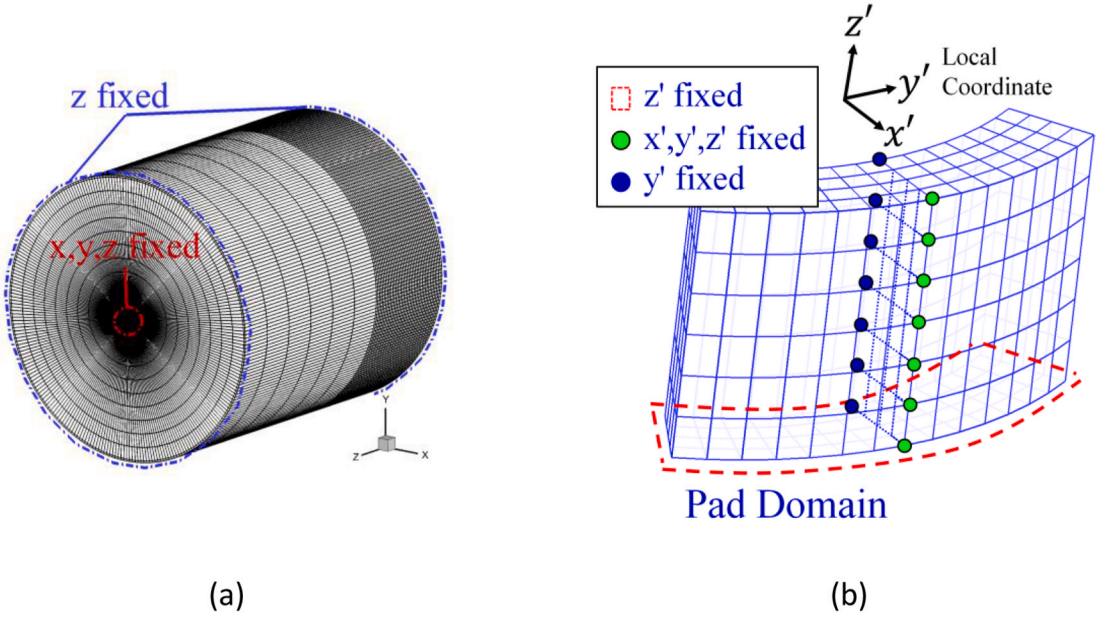

Fig. 6. Illustration of prescribed boundary conditions for the FEA solver; (a) shaft domain, (b) pad domain.

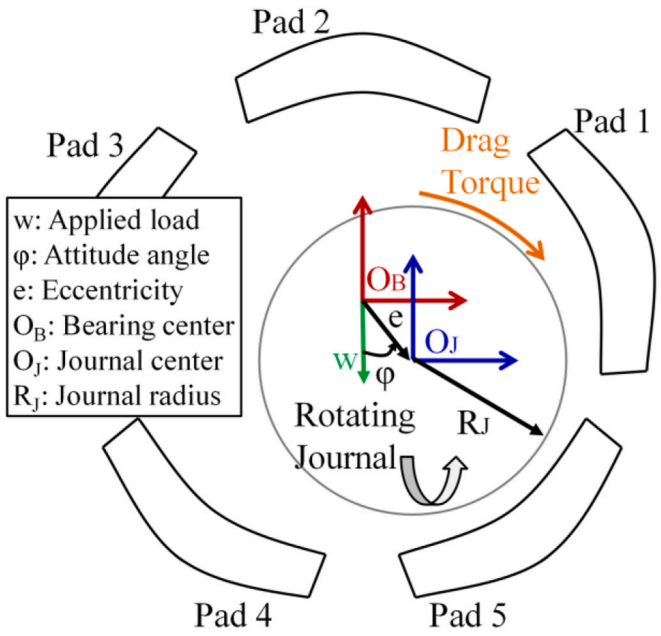

Fig. 8. Pad Numbering and Bearing Geometric Features in 3D CFD model.

interface boundary location values.

The CFD code adopts an iterative algebraic solver for all governing equations, and the mesh deformation, degree of freedom motion (dof) boundary conditions are periodically updated in the global iteration loop. For instance, the mesh deformation boundary position conditions from pad tilting motion are updated every 20 iterations. The shaft translational motion, pad pivot motion, and solid deformations updates for the mesh deformation boundary position conditions occur every 100, 500, and 1000 iterations, respectively. Convergence criteria include (1) variable's residuals are below 1.e−6, (2) all monitored parameters including domain peak temperature and domain averaged temperature are sufficiently converged, (3) iteration increments of all updated displacements for the mesh deformation equation are near zero. The computations are ended when the convergence criteria are satisfied.

3.2. Governing thermal-fluid equations

The CFD governing equations for flow and heat transfer are summarized here. The flow regime can be turbulent in certain locations and operating speeds. The Reynolds Averaged Navier-Stokes (RANS) equation is applied for the momentum equation, to consider the statistically averaged turbulence effect in the time domain. The RANS equation with the eddy viscosity hypothesis applied to the Reynolds stress term, yield the steady-state continuity and momentum equations expressed in Eqs. (1) and (2), where ρ_f is the fluid density, p' is the modified pressure determined from summing the static pressure (p) and $2/3\rho_f k$, k is the turbulent kinetic energy dependent variables, μ_{eff} is the effective viscosity defined by summing the dynamic viscosity (μ_f) and the turbulent (eddy) viscosity (μ_t), and u_i is the velocity of the fluid.

Continuity and momentum equations (p, u_i):

$$\frac{\partial}{\partial x_i}\left(\rho_f u_i\right) = 0 \tag{1}$$

$$\frac{\partial}{\partial x_j}\left(\rho_f u_i u_j\right) = -\frac{\partial p'}{\partial x_i} + \frac{\partial}{\partial x_j}\left[\mu_{eff}\left(\frac{\partial u_i}{\partial x_j} + \frac{\partial u_j}{\partial x_i}\right)\right] \tag{2}$$

The thermal flow model is desired for TPJB performance prediction,

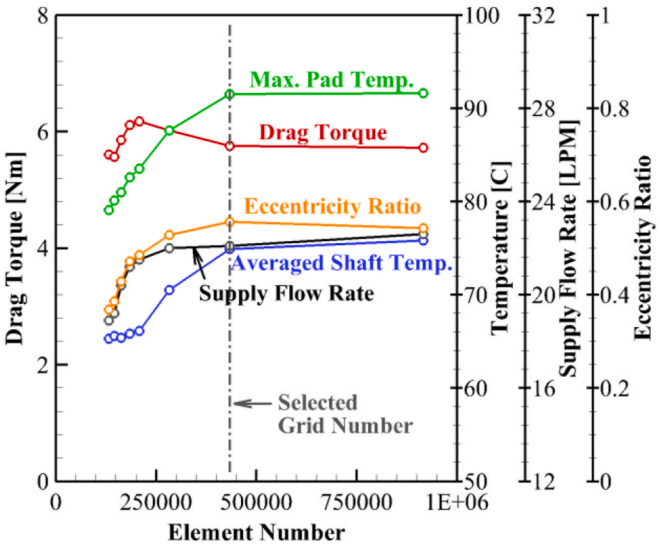

Fig. 10. Grid Independence Summary conducted for a smooth TPJB with a 5000 N load and 13,000 RPM speed.

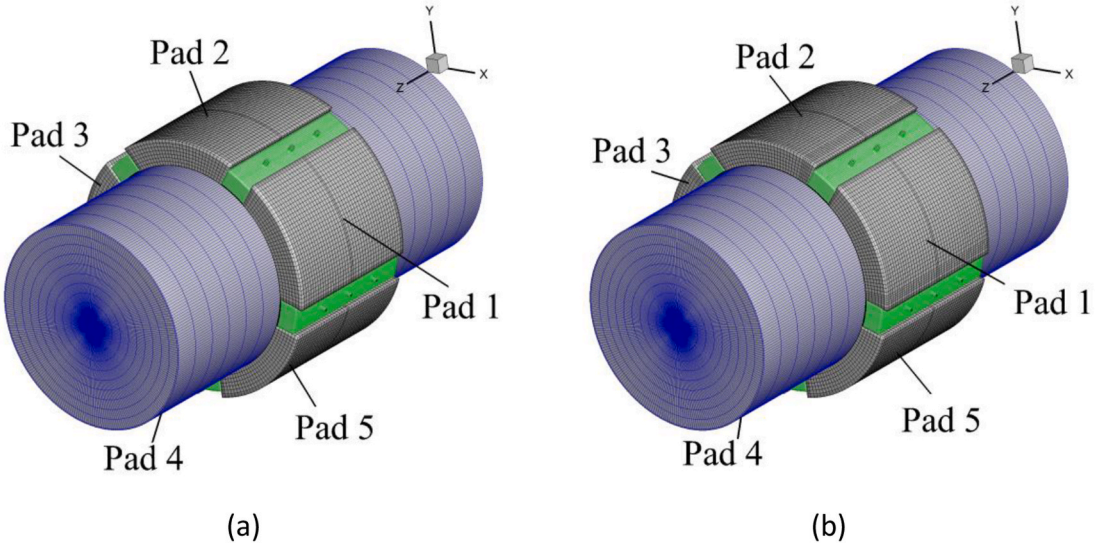

Fig. 9. Geometry and mesh for TPJBs; (a) smooth TPJB, (b) pocketed TPJB

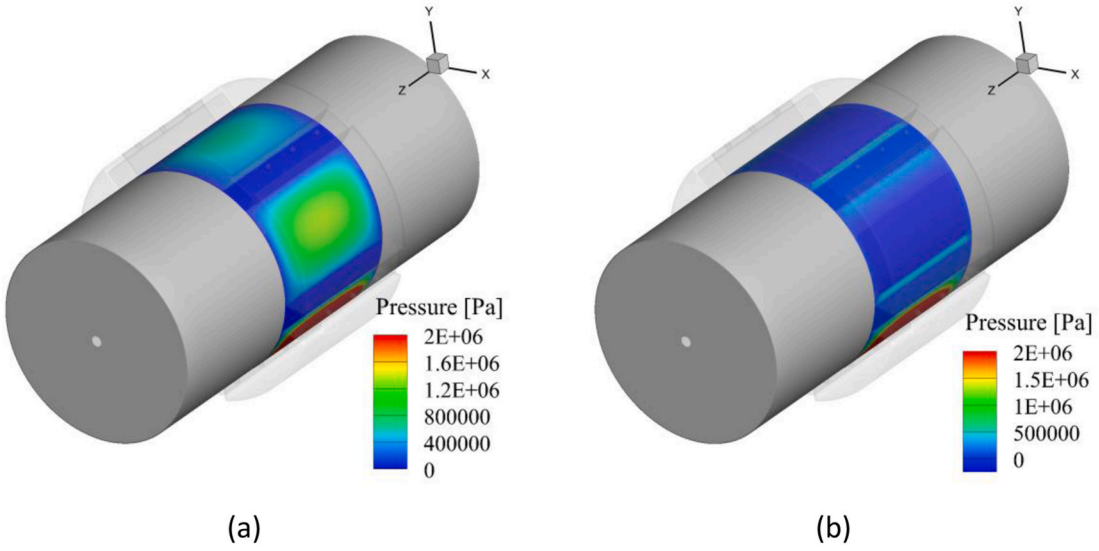

Fig. 11. Pressure Contour (10,000 N load, 9000 rpm) by CFD simulation; (a) Smooth TPJB, (b) Pocketed TPJB.

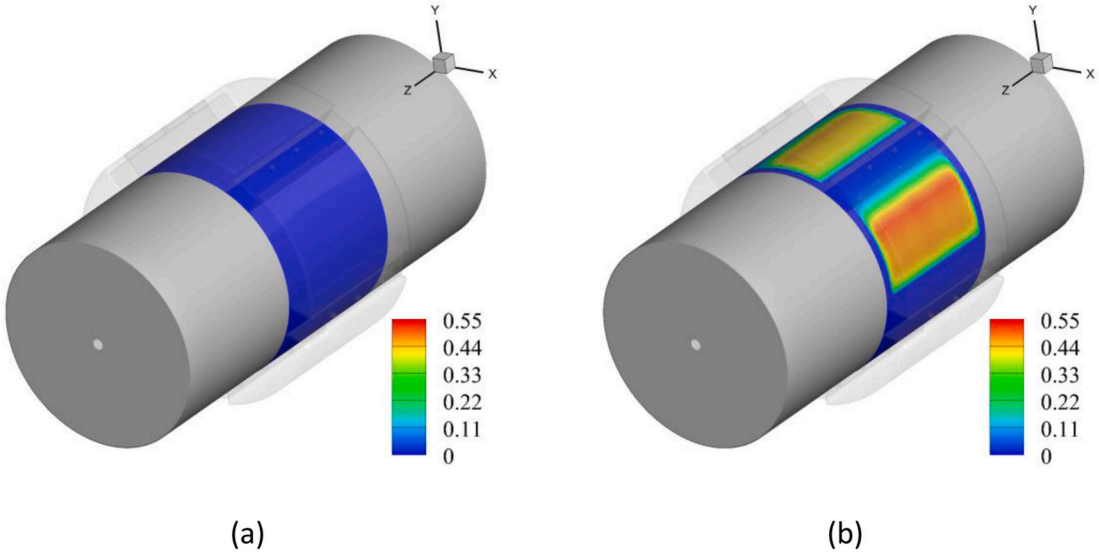

Fig. 12. Vapor Volume Fraction Contour by CFD simulation (10,000 N load, 9000 rpm); (a) Smooth TPJB, (b) Pocketed TPJB.

because the dynamic viscosity is an exponential function ($\mu_f = \alpha_v \exp(-\beta_v(T_f - T_{ref}))$) of the fluid temperature (T_f), and it affects both momentum and energy equation solutions. The constants α_v, β_v, and T_{ref} are 0.0342 [Pa · s], −0.0308, and 40 [°C], respectively, in the CFD simulation. The Reynolds averaged energy equation in the fluid domain is given by Eq. (3). The equation includes convective, diffusive, and source terms, and the final source term on the right-hand side is the viscous heat dissipation, which equals the drag power loss of the TPJB. The parameter λ_f is the thermal conductivity, and the h_{tot} is the total enthalpy, including the static enthalpy and kinetic energy.

Fluid Energy Equation (T_f):

$$\frac{\partial}{\partial x_j}\left(\rho_f u_j h_{tot}\right) = \frac{\partial}{\partial x_j}\left(\lambda_f \frac{\partial T_f}{\partial x_j}\right) + \frac{\partial}{\partial x_j}\left[u_i\left(-p'\delta_{ij} + \mu_{eff}\left(\frac{\partial u_i}{\partial x_j} + \frac{\partial u_j}{\partial x_i}\right)\right)\right] \tag{3}$$

The 2-equation, k - ω based Shear Stress Transport (SST) turbulence model, is employed in this research. The baseline (BSL) k-omega model is derived from combining the k-omega and k-epsilon turbulence models with blending function to overcome the drawbacks of k-omega (sensitivity to freestream conditions) and k-epsilon (difficulty on near-wall treatment for low-Reynolds number) models. In the baseline model, the eddy-viscosity is further modified by a limiter to account for the Shear Stress Transport (SST), which is the k-omega based SST model. The k-omega based SST model is applied in this study due to its accuracy at low-Reynolds number, and wall-function flexibility (automatic wall-function) for the near-wall mesh treatment. The Reynolds number is low over the entire fluid domain, and this turbulence model's validity for the flow with the low-Re number has been confirmed in prior studies [16–18]. The turbulent kinetic energy (k) and turbulent frequency (ω) fields are obtained by solving Eqs. (4) and (5), and the solutions are used to determine the turbulent (eddy) viscosity (μ_t) in Eqs. (2) and (3).

Turbulent kinetic energy (k):

$$\frac{\partial}{\partial x_j}\left(\rho_f u_j k\right) = \frac{\partial}{\partial x_j}\left[\left(\mu_f + \frac{\mu_t}{\sigma_{k3}}\right)\frac{\partial k}{\partial x_j}\right] + P_k - \beta'\rho_f k\omega \tag{4}$$

Turbulent frequency (ω):

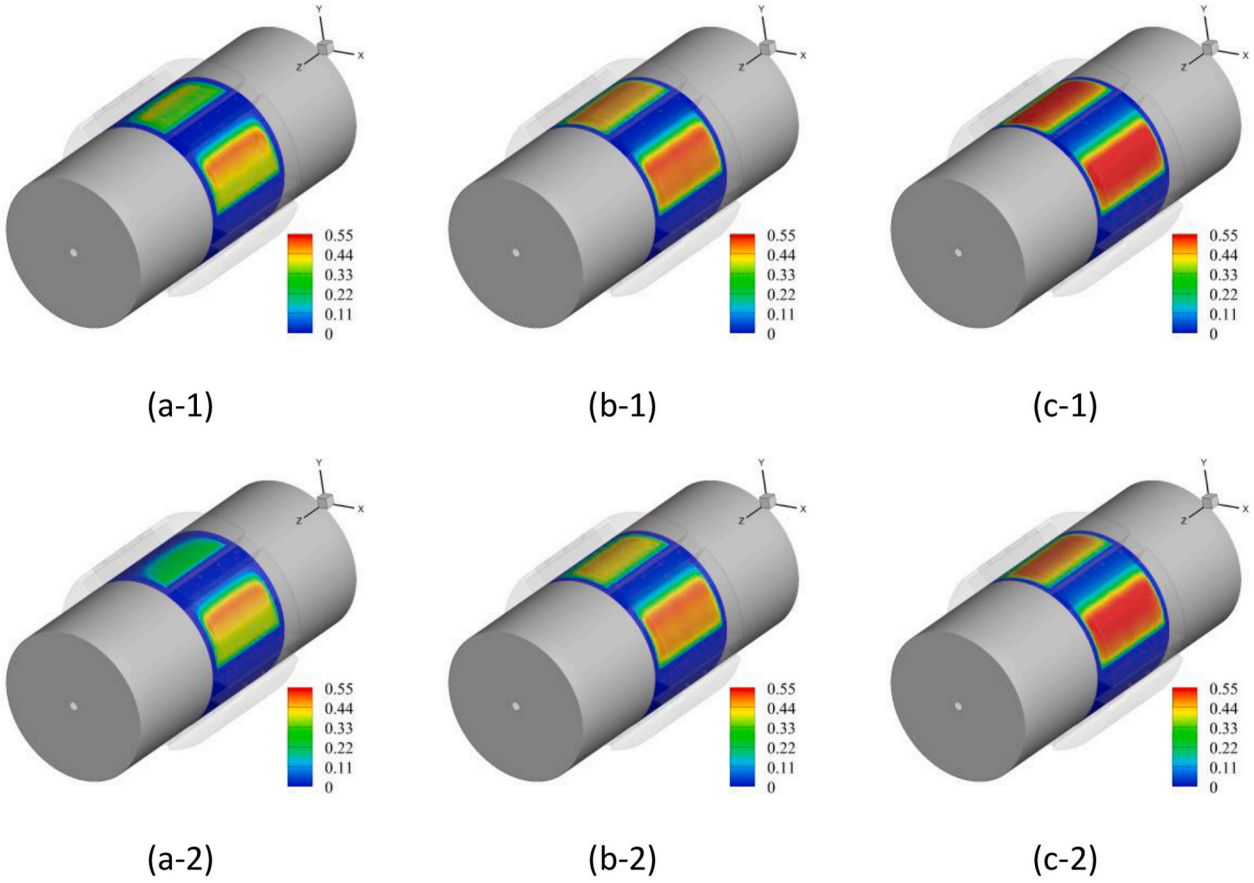

Fig. 13. Vapor volume fraction contour with applied load and operating speed changes; (a) 5000 RPM, (b) 9000 RPM, (c) 13,000 RPM; (1) 5000 N, (2) 15,000 N.

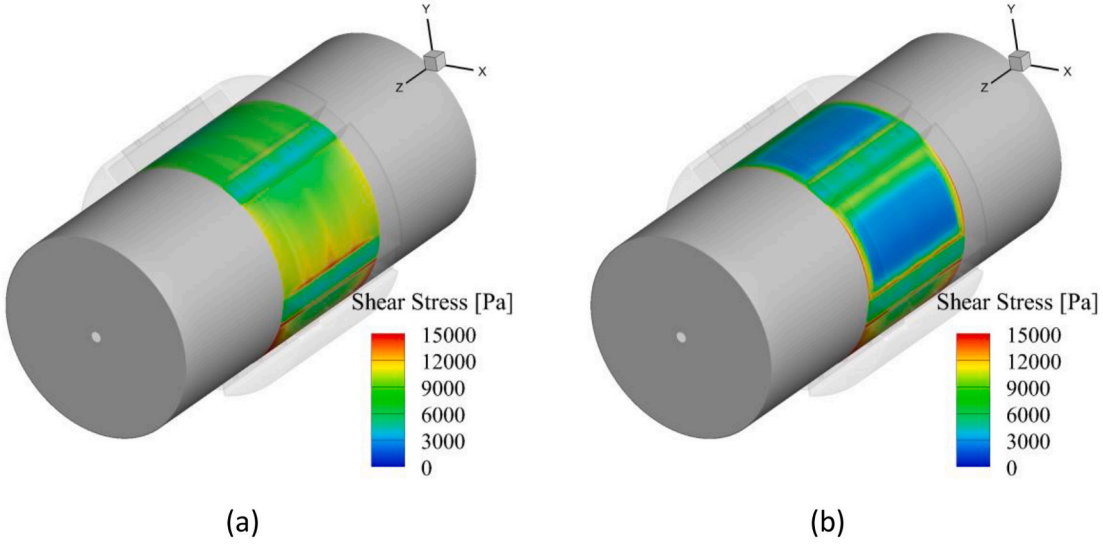

Fig. 14. Shear Stress Contour by CFD simulation (10,000 N load, 9000 rpm); (a) Smooth TPJB, (b) Pocketed TPJB.

$$\frac{\partial}{\partial x_j}\left(\rho_f u_j \omega\right) = \frac{\partial}{\partial x_j}\left[\left(\mu_f + \frac{\mu_t}{\sigma_{\omega 3}}\right)\frac{\partial k}{\partial x_j}\right] + (1-B_1)2\rho_f \frac{1}{\sigma_{\omega 2}\omega}\frac{\partial k}{\partial x_j}\frac{\partial \omega}{\partial x_j} + \alpha_3 \frac{\omega}{k} P_k - \beta_3 \rho_f \omega^2 \tag{5}$$

where β' is 0.09, and $\sigma_{\omega 2}$ is 1/0.856. σ_{k3}, $\sigma_{\omega 3}$, α_3, and β_3 are calculated by the blending function B_1 and some constants, and P_k is the turbulence production term [19]. The blending function includes the wall distance variable from the nearest wall to the cell, requiring solution of an additional wall distance equation. An automatic wall function is applied, which can account for the viscous or inertia sublayer depending on the first cell distance from the wall.

The flow regime between the journal and pad is mainly laminar because of the thin film thickness relative to the journal radius. The groove region between the pads can be turbulent depending on the operating speed. The gamma transitional turbulence model is utilized to

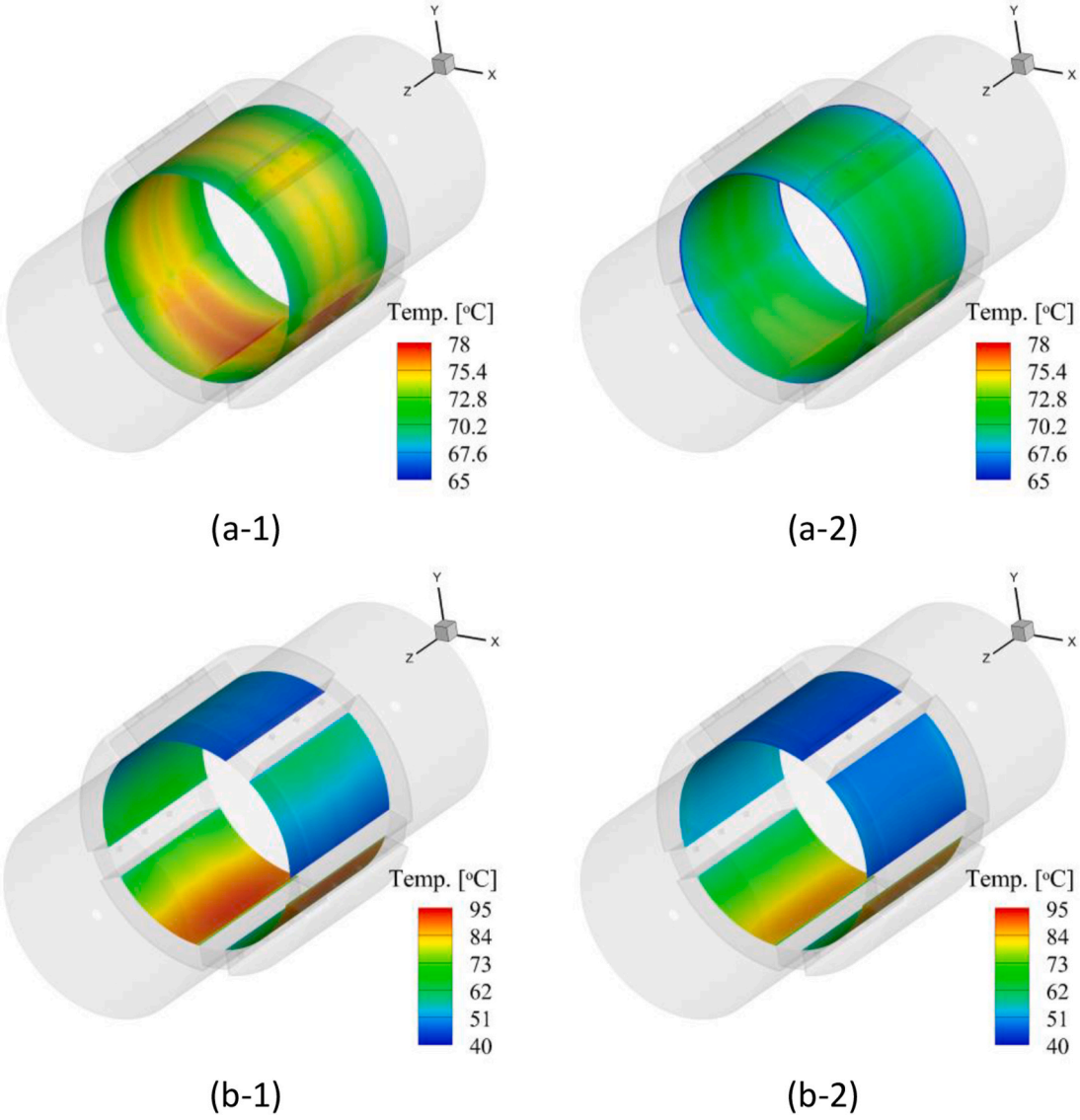

Fig. 15. Temperature Contour by CFD simulation (10,000 N load, 9000 rpm); (a) Journal Surface, (b) Pad Surface; (1) Smooth TPJB, (2) Pocketed TPJB.

account for the laminar and turbulent flow regimes with transitions.

Turbulent Intermittency (γ):

$$\frac{\partial(\rho_f u_j \gamma)}{\partial x_j} = \frac{\partial}{\partial x_j}\left[\left(\mu_f + \frac{\mu_t}{\sigma_\gamma}\right)\frac{\partial \gamma}{\partial x_j}\right] + P_{\gamma 1} - E_{\gamma 1} + P_{\gamma 2} - E_{\gamma 2} \tag{6}$$

where σ_γ is 1.0, and the source terms ($P_{\gamma 1}$, $E_{\gamma 1}$, $P_{\gamma 2}$, $E_{\gamma 2}$) are determined mainly by the transition onset Reynolds number. The turbulent intermittency (γ) is obtained by solving (6), and the gamma solutions (γ) interact with the source terms of the turbulent kinetic energy (4) to simulate the adaptable flow regimes.

Laminar and turbulent flow regimes can coexist in a tilt pad journal bearing, since the thin-film flow is mostly laminar, but the flow between pads is often turbulent due to the relatively large geometric dimensions, and strong nozzle/orifice injection flows, such as with direct lubrication. The flow regime modeling uncertainty is reduced by employing a transitional turbulence model. A laminar model may save 30–40% in computational time per computational iteration, however numerical instability has been observed in the groove regions between pads, at high local Reynolds numbers. Although converged solutions can be obtained with a laminar assumption, the time saving may not be significant, since the solution requires more computational iterations when high Reynolds numbers occur between pads. Thus, a transitional turbulence model is utilized to address accuracy, numerical stability, and computational time, in the dual flow regime bearing model.

Phase change inside the pockets is an important phenomenon that needs to be calculated in the CFD simulation. As described in Sec. 2, vaporization (cavitation) starts at the leading edge of the pockets, and the fluid undergoes condensation by returning to the liquid phase. The multiphase flow is modeled by the mixture assumptions that all fluid phases share the momentum, turbulence, and energy equations in the fluid domain. The continuity equation for phase α is solved for its volume fraction (r_α).

Phase α Continuity Equation (r_α):

$$\nabla \cdot (r_\alpha \rho_\alpha u_\alpha) = \dot{m}_\alpha \tag{7}$$

The source term ($\dot{m}_\alpha$) is the mass transfer between the liquid and gas phases. The mass transfer can be derived based on the Rayleigh-Plesset model, which considers bubble dynamics. The Reynolds cavitation model over-simplifies the mass transfer rate and neglects mass continuity. Therefore, conventional approaches are not employed in the TPJB simulations.

The mass transfer rate for a cavitated region is governed by the bubble dynamics equation (8), which is derived from the generalized

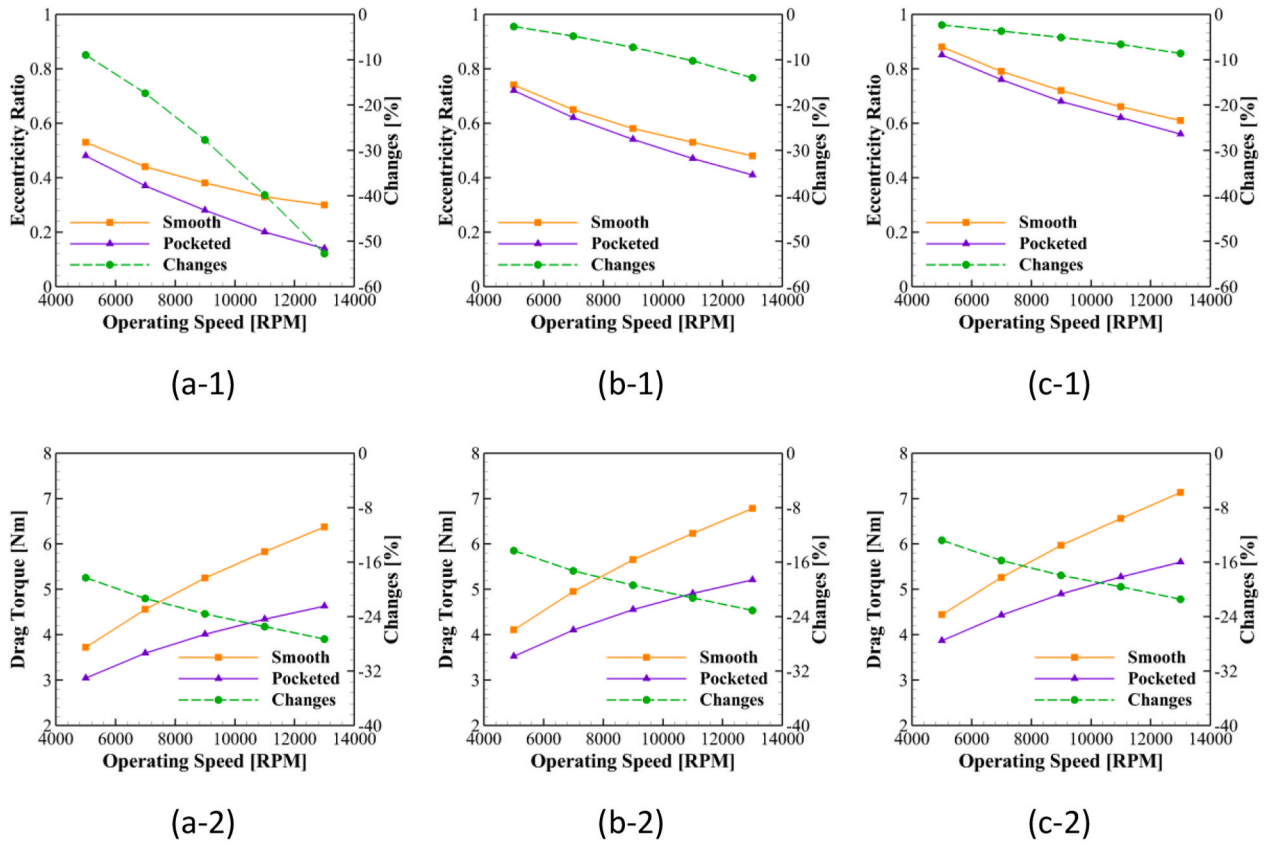

Fig. 16. Eccentricity Ratio and Drag Torque Reductions with Pocketed TPJB according to applied load (w); (a) w = 5000 N, (b) w = 10,000 N, (c) w = 15,000 N; (1) Eccentricity Ratio, (2) Drag Torque.

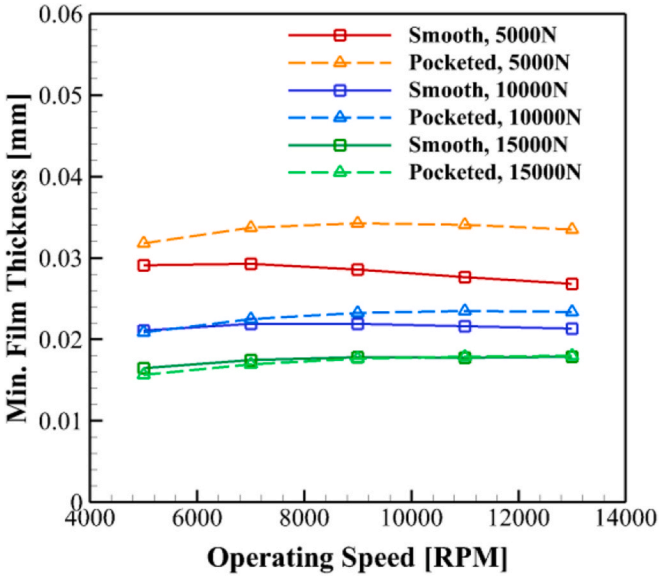

Fig. 17. Minimum Film Thickness vs Operating Speed and Static Load.

Rayleigh-Plesset equation.

$$R_{bb}\frac{d^2R_{bb}}{dt^2}+\frac{3}{2}\left(\frac{dR_{bb}}{dt}\right)^2+\frac{2\sigma}{\rho_f R_{bb}}=\frac{p_{cav}-p}{\rho_f} \tag{8}$$

where σ and R_{bb} are the surface tension coefficient and bubble radius, respectively, and p_{cav} indicates the saturation pressure. Neglecting second-order and surface tension terms in Eq. (8) yields the simplified form

$$\frac{dR_{bb}}{dt}=\sqrt{\frac{2}{3}\frac{p_{cav}-p}{\rho_f}} \tag{9}$$

Then, the bubble mass change rate is expressed by

$$\frac{dm_{bb}}{dt}=\rho_v\frac{dV_{bb}}{dt}=4\pi R_{bb}^2\rho_v\frac{dR_{bb}}{dt}=4\pi R_{bb}^2\rho_v\sqrt{\frac{2}{3}\frac{p_{cav}-p}{\rho_f}} \tag{10}$$

where V_{bb} is the bubble volume with a sphere shape. The bubble mass change rate per unit volume can be expressed with Eq. (10), an empirical calibration constant (C_F), and the bubble number per unit volume ($N_{bb} = r_v/V_{bb}$), as

$$\dot{m}_v=C_F N_{bb}\frac{dm_{bb}}{dt}=C_F\frac{3\rho_v r_v}{R_{bb}}\sqrt{\frac{2}{3}\frac{p_{cav}-p}{\rho_f}} \tag{11}$$

With further modifications suggested by Zwart et al. [Ref. 20], the final forms of the mass transfer rates for vaporization and condensation are given by

$$\dot{m}_v=C_{F,evap}\frac{3\rho_v r_{nuc} r_l}{R_{bb}}\sqrt{\frac{2}{3\rho_l}(p_{cav}-p)},\ \ if\ p_{cav}>p\ \ \text{(Vaporization)} \tag{12}$$

$$\dot{m}_l=C_{F,cond}\frac{3\rho_v r_v}{R_{bb}}\sqrt{\frac{2}{3\rho_l}(p-p_{cav})},\quad if\ p_{cav}<p\ \ \text{(Condensation)} \tag{13}$$

where R_{bb}(2 nm) and r_{nuc}(5e-4) are the bubble radius and the volume fraction of the nucleation site, respectively, and $C_{F,evap}$(50) and $C_{F,cond}$(0.01) are empirical phase change parameters. The parameters of the mass transfer rates are the default values given in the commercial

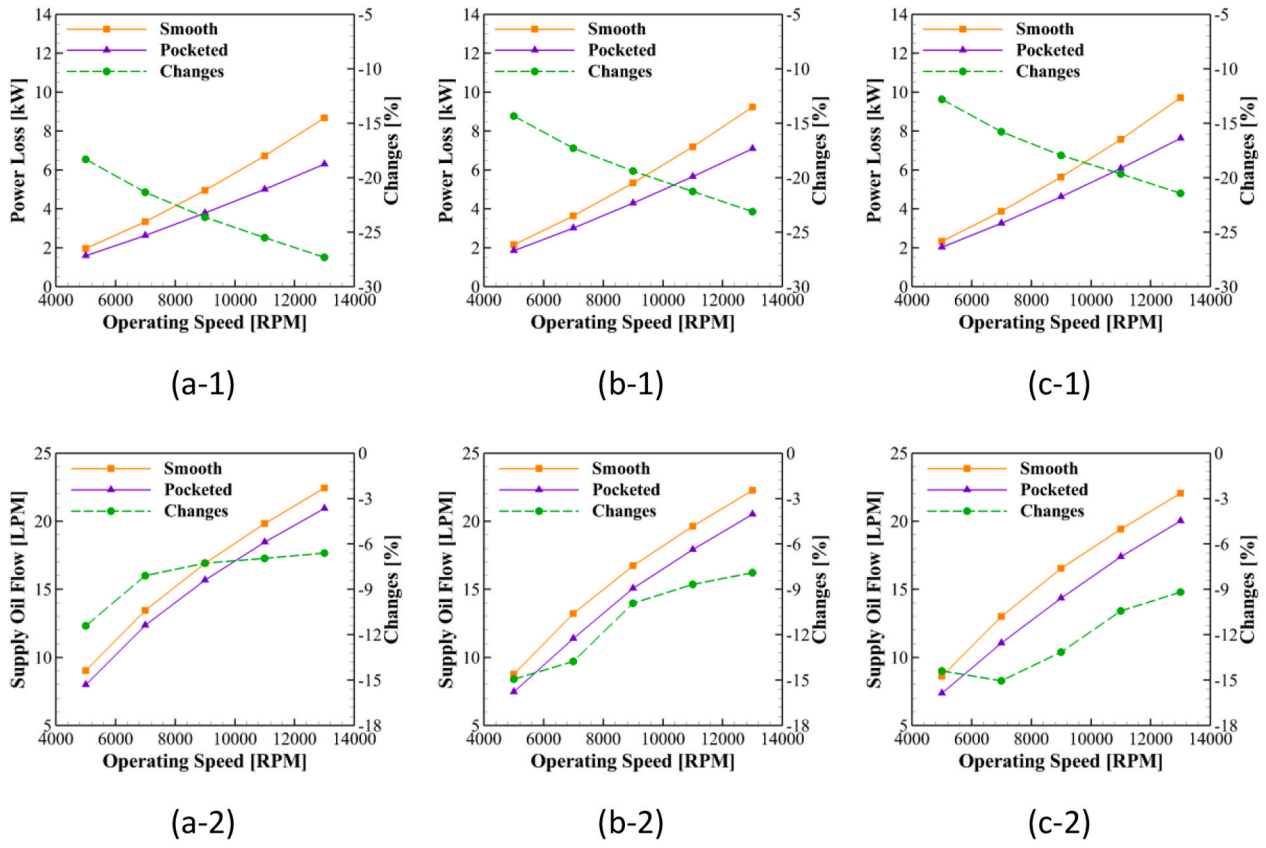

Fig. 18. Power Loss and Supply Oil Flow Benefits of Pocketed TPJB according to applied load (w); (a) w = 5000 N, (b) w = 10,000 N, (c) w = 15,000 N; (1) Power Loss, (2) Supply Oil Flow.

software. Vaporous cavitation results from a phase change occurring when local pressure drops below saturation. Vaporous cavitation is mainly modeled with the Rayleigh-Plesset approach. Gaseous cavitation results when dissolved gas like air is released due to a decrease in pressure. Very few theoretical models on gaseous cavitation have been proposed, considering gas solubilities and equilibrium assumptions between the gas partial pressure and fluid pressure [21]. Gaseous cavitation is not included in the present model, but will be included in future work. Thus, the bubble formation in the present model is affected only by the vaporous cavitation mechanism described in Eq. (12).

This heat flow in the fluid is dominated by the fluid advection flow exiting to the side outlet. Some of the viscous heat generated in the fluid film flows to ambient through the shaft and pads, affecting their temperatures. Calculating the solid temperatures is essential since the resulting thermal deformations affect the film thickness, which affects the TPJB performance. Accordingly, the heat conduction equation needs to be solved for the solid domains, and the governing equations are written in Eqs. (14) and (15). Note that the convection term in the shaft energy equation is included for the shaft rotation effects in the fixed frame.

Shaft Energy Equation (T_s):

$$\frac{\partial}{\partial x_i}\left(\rho_s u_s h_{tot,s}\right) = \frac{\partial}{\partial x_i}\lambda_s \frac{\partial T_s}{\partial x_i} \tag{14}$$

Pad Energy Equation (T_s):

$$0 = \frac{\partial}{\partial x_i}\lambda_p \frac{\partial T_p}{\partial x_i} \tag{15}$$

u_s is the shaft rotating speed at each element, and it is calculated by multiplying the element radial location (R_e) and angular velocity (w_s).

The displacements of the shaft translational x and y motions, pad tilting and pad pivot motions shown in Fig. 2(b) are periodically updated during the Newton-Raphson driven search for the equilibrium states. These displacements are applied to the interface boundaries of the mesh deformation equation between the journal and fluid-film and between the pad and fluid-film [16]. Likewise, the displacement solutions in the structure solver modify the interface boundary conditions to include effects of the solid thermal-elastic deformations, and shaft centrifugal force deformations. The mesh deformation equation is expressed in Eq. (16), where the dependent variable is the mesh displacement (δ_i) relative to the initial node location. The mesh stiffness (Γ_{dis}) is chosen with any constant value to maintain the mesh orthogonal quality and induce uniform mesh deformations in the film thickness direction.

Mesh Deformation Equation (δ_i):

$$\frac{\partial}{\partial x_i}\Gamma_{dis}\frac{\partial \delta_i}{\partial x_i} = 0 \tag{16}$$

3.3. Boundary condition

Fig. 5 shows the prescribed boundary conditions for the CFD solver. The interface boundaries between the journal and the fluid-film and between the pad and the fluid-film are also defined in the CFD solver. For stable convergence, the supply oil inlet is prescribed with total pressures in the continuity and momentum equations, where the total pressure is the sum of the static and dynamic pressures. Ambient pressure is imposed at the side oil outlet. The interface boundaries between the pad and fluid-film (including the step and pocket surfaces) are prescribed with a no-slip wall condition, and a moving wall boundary condition is applied to the interface boundary between the journal and fluid-film, due to the spinning journal. A 5% turbulence intensity is assumed at the supply, and zero gradient turbulence boundary conditions are prescribed at the side oil inlet. The vapor volume fractions are

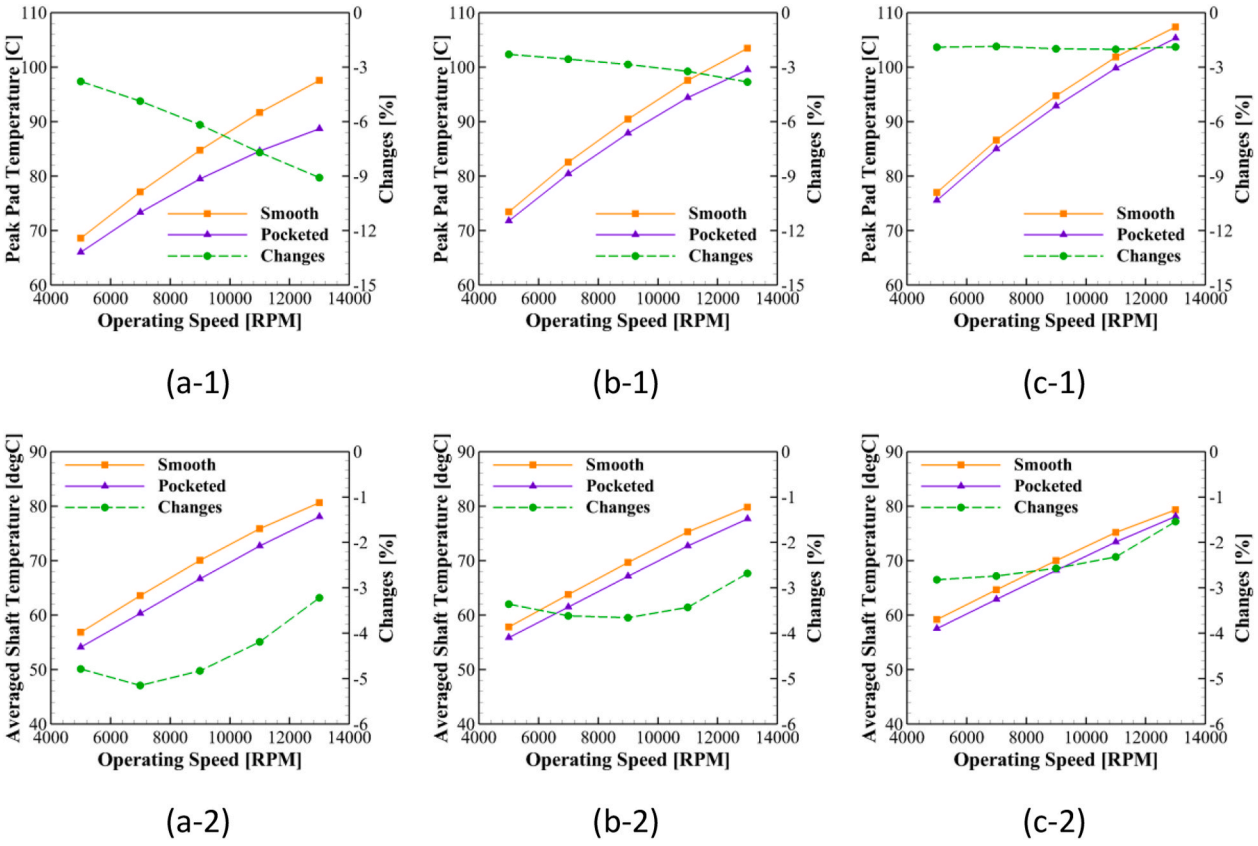

Fig. 19. Peak Pad and Averaged Shaft Temperature Benefits of Pocketed TPJB according to applied load (w); (a) w = 5000 N, (b) w = 10,000 N, (c) w = 15,000 N; (1) Peak Pad Temperature, (2) Averaged Shaft Temperature.

set to zero at all inlet and outlet boundary conditions.

A 40 degC oil temperature is applied at the supply oil inlet and the side outlet for the energy equations. Heat convection boundary conditions, with heat convection coefficients and surrounding temperatures, are applied on the shaft, pad, and groove outer surfaces. All interface boundaries between the journal and fluid-film and between the pad and fluid film take the displacement values for all shaft and pad dofs and the thermal-elastic deformations. Fig. 6 illustrates the prescribed boundary conditions in the FEA solver. Symmetry boundary conditions are imposed by applying zero displacements in the z direction. As shown in Fig. 6(b), the additional y'-constraints in the middle of the inner pad surface are taken to make a solvable problem. The pad pivot boundaries are fixed in the x', y', and z' directions. Displacements from the nonlinear pivot stiffness are calculated separately in a Python-based code [16].

4. Results and discussion

4.1. Geometry, meshing and input conditions

The original TPJB is referred to as "Smooth TPJB," and the proposed TPJB with the pockets and steps is referred to as "Pocketed TPJB". The benefits of the latter are demonstrated by comparing the predicted performances of the Smooth TPJB and Pocketed TPJB. Validations for the CFD-TEHD and cavitation models were conducted, as reported in the Appendix, as a precursor to the CFD based comparison of the smooth and pocketed bearings. The geometry, mesh, and CFD input parameters of the example TPJB are given in Table 1. The CFD simulations showed similar levels of benefit for TPJBs with different diameters, lengths, and lubrication types. The diameter and length considered in the example are 80 mm and 60 mm, respectively. Each CFD-FEA TEHD simulation requires 105 wall clock hours utilizing 12 cores of a computer server based on the dual Intel Xeon 2.5 GHz E5-2670 v2 10-core processors, in the TAMU High Performance Research Computing Center (HPRC).

Based on extensive CFD simulation studies, the pocket and step are designed to have the cavitation region as wide as possible and enough land to produce the pressure to stabilize the pads. The specific pocket and step geometries are illustrated in Fig. 7. Both pocket and step have 10 mm depth, and the pocket has a much larger circumferential length than the step, as described in Sec. 2. The axial length of the pocket and step is 53 mm, which is approximately 88% of the TPJB length. The pocket and step are implanted in the upper pads (Pad1, Pad2, and Pad3), and the case of only a single pocketed pad (Pad 2) is also presented in Sec. 4.2.

A wide range of applied load (5–15 kN) and operating speed (7–13 kRPM) cases were simulated to investigate the pocket and step effects for the various eccentricity ratios and journal surface velocities. Fig. 8 illustrates the eccentricity ratio (ε) and attitude angle (ϕ). Both smooth and pocketed TPJBs always predict a zero attitude angle, and so this result is not presented for individual cases. The eccentricity ratio can be expressed as

$$\varepsilon = \frac{e}{C_{l,b}} \tag{17}$$

The primary purpose of the novel TPJB design is to reduce the drag torque acting opposite to the rotation direction, as seen in Fig. 8. The mathematical expressions of the drag torque (DT) and power loss (PL) are given in Eqs. (18) and (19), respectively.

$$DT = \int_{A_s} \left(R_s \times \mu_f \frac{\partial u_{cir}}{\partial r} \right) dA_s \tag{18}$$

$$PL = DT \times \omega_s \tag{19}$$

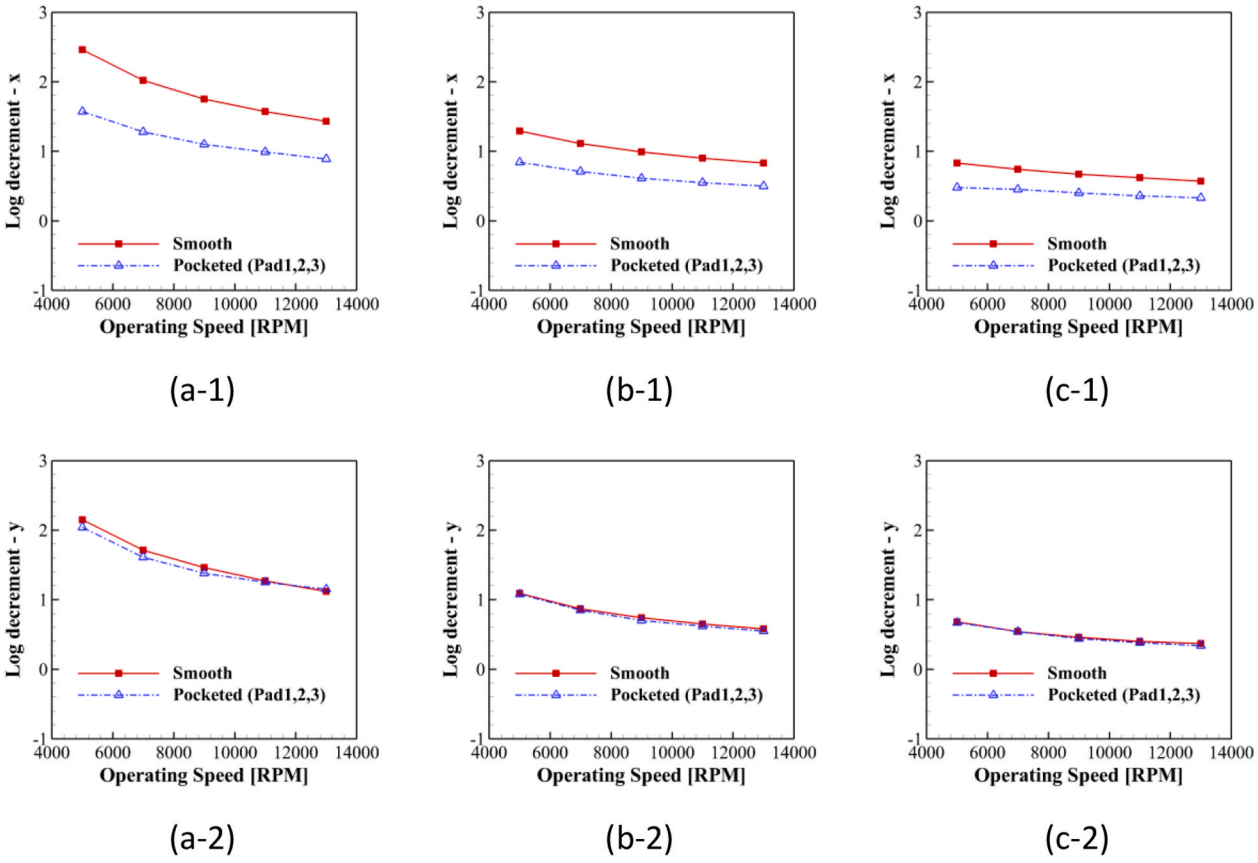

Fig. 20. x and y log decrements for evaluation of the dynamic performance; (a) w = 5000 N, (b) w = 10,000 N, (c) w = 15,000 N; (1) Log decrement-x, (2) Log decrement-y.

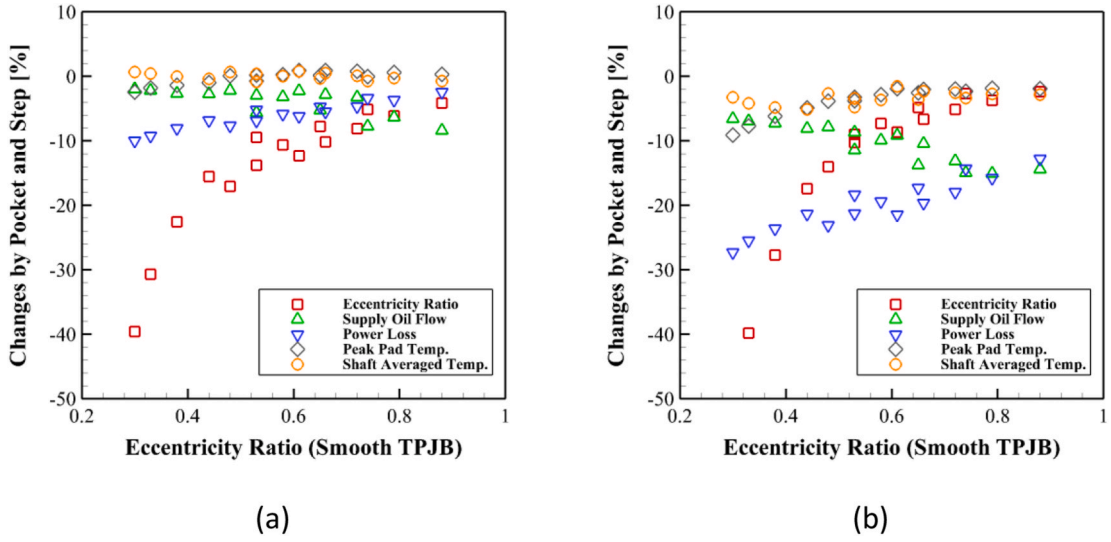

Fig. 21. Benefits of Pocketed TPJB expressed by Eccentricity Ratio of Smooth TPJB; Pocket and Step Locations: (a) Pad2, (b) Pad1, Pad2, and Pad3.

where R_s is the shaft radius, A_s is the journal surface area, u_{cir} and ω_s are the circumferential velocity and rotation speed, respectively.

As described earlier, the shaft, pad, and fluid domains are considered in the CFD simulation. Fig. 9 depicts the modeled TPJB with the mesh for the smooth and pocketed TPJB. A mesh independence study was conducted on the Thermo-Hydrodynamic (THD) Model, and is summarized in Fig. 10. The number of elements was selected to be 433,436 based on the results in Fig. 10 and the corresponding computation times. The final mesh was identical for the smooth and pocketed bearings as illustrated in Fig. 9.

4.2. *The effect of multiple pockets and steps on upper pads*

Comparison between the simulation results for the smooth and pocketed TPJBs demonstrates the benefits of the latter. Fig. 11 shows the pressure contours when the pockets are installed on pad1, pad2, and

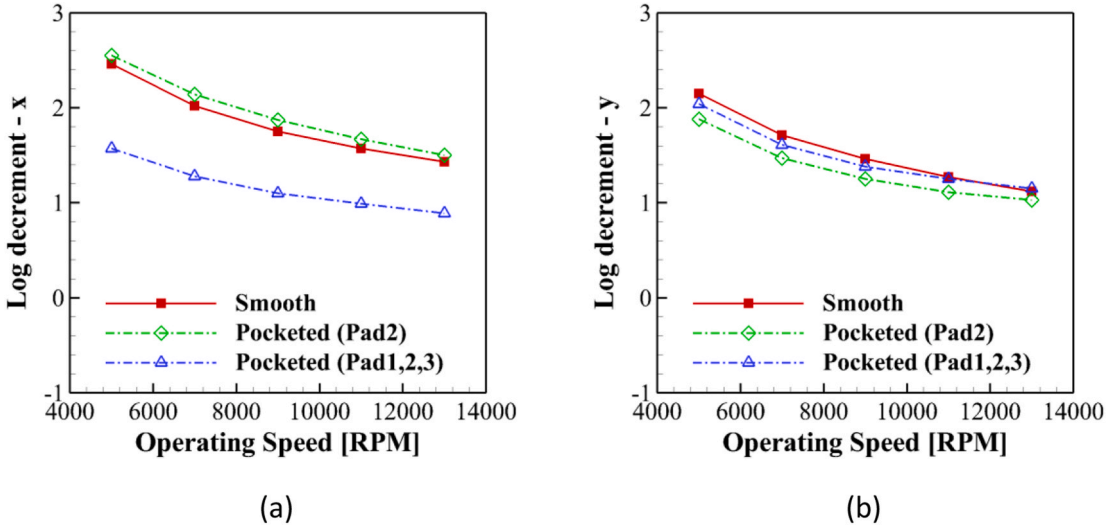

Fig. 22. x and y log decrements for evaluation of dynamic performance (5000 N); Pocket and Step Locations: (a) log decrement – x, (b) log decrement – y.

pad3 of the pocketed TPJB. The color contour levels are adjusted to focus on the pressure distribution of the upper pads, since their pressures are much lower than that in the bottom pads.

As shown in Fig. 11(b), the peak pressures in the pocketed TPJB are produced at the step and pocket trailing edges, which helps stabilize the pad tilting motion. The pressure is suddenly decreased in the circumferential direction where the film thickness is suddenly increased, to conserve fluid momentum. Thus, the pressure suddenly drops at the leading edge of the pockets, generating cavitation in the pocket. The negative gauge pressure inside the pockets is recovered at the trailing edge of the pocket. In addition, Fig. 12(b) shows that the negative pressure inside the pockets causes the significant phase change (high vapor volume fraction) from the liquid phase to the gas phase, while cavitation is not observed in the smooth TPJB result, as seen in Fig. 12 (a).

The vaporization is activated more at the higher speeds, as demonstrated in Fig. 13, because the pressure drop inside the pockets becomes larger at the higher speeds. Fig. 13 also shows that the degree of cavitation is nearly insensitive to the applied load. Further simulations have demonstrated that a high level of cavitation occurs for a wide range of operating conditions. This is good since it suggests that the proposed novel features for the TPJB may be beneficial for a wide range of applications.

In the pockets, the evaporation significantly lessens the dynamic viscosity (μ_f) of the fluid, and the larger film thickness decreases the velocity gradient ($\partial u_{cir}/\partial r$). Therefore, the pockets reduce the shear stress ($\mu_f \ \partial u_{cir}/\partial r$). A substantial shear stress reduction is confirmed in Fig. 14, which implies a corresponding significant drop in drag torque and power loss by Eqs. (18) and (19), respectively. Fig. 14(a) shows a significant level of shear stress on the upper pads of the conventional TPJB despite the low pad loading. So, reducing the power loss from the upper pads can yield a significant overall power savings for the TPJB.

Fig. 15 shows the temperature distribution on the pad and journal at 9000 rpm and 10,000 N load, for both the smooth and pocketed bearings. Figs. 15(a-1) shows the temperature varying in the axial direction due to the three nozzle oil injection cooling flows. The pad surface temperature increases along the rotation direction, and the bottom pads have relatively higher temperatures because of the larger viscous heat generation in the thinner film. As shown in Fig. 15, the overall temperature at both pad and journal surfaces is decreased in the pocketed TPJB.

Fig. 11 shows that the negative gauge pressure in the pockets yields a lower load condition on the upper pads, than for the smooth TPJB. Thus, the journal lifts to the opposite direction of the applied load, and the eccentricity ratio is decreased, with an increase in the minimum film thickness. This indicates the pockets can provide power loss reduction benefits without sacrificing bearing load capacity. The eccentricity ratio is increased with increasing applied load, and decreased with increased operating speed, as shown in Fig. 16. The percent eccentricity ratio reductions from the pocketed TPJB are increased with increased speed and with decreased applied loads, resulting from the increased proportion of the upper pad loads, with respect to the bottom pad loads.

Fig. 17 shows that the pockets tend to raise the shaft, decreasing eccentricity ration and increasing minimum film thickness for a given static load. The increase in minimum film thickness is more pronounced at low loads (5000 and 10,000 N) than at high loads (15,000 N).

TPJB drag torque and power loss are significantly reduced by the pocket cavitation, when applying the pocket and step on the upper pads, as seen in Fig. 16(2) and Fig. 18(1). Mathematical expressions of the drag torque and power loss are given in Eqs. (18) and (19). Power loss follows the same trends as the drag torque by Eq. (18). The drag torque and its benefits are not highly sensitive to applied load, but are for operating speed (RPM). This indicates the proportion of the drag torque caused by the upper pads becomes higher at the high speeds, when compared to that at the bottom pads. The drag torque and power loss reductions achieved range from $-12.8 \sim -27.3\%$, and are very distinguishable at higher operating speeds, independent of applied load.

Fig. 18(2) shows the predicted supply oil flow rate for the given total pressure inlet boundary condition. The supply oil flow rate increases with operating speed due to the increase of the side leakage flow and total pressure at the supply oil inlet. The cavitation inside the pockets allows the TPJB to operate with a reduced oil flow rate for the upper pads. It is confirmed that the required flow rate is significantly reduced with the pocket and step included. This has the practical advantage of derating the required oil supply pump, reducing cost and power.

There is a limit on recommended pad surface operating temperatures due to the material's (Babbitt) melting temperature and fatigue life. Thus, it is desirable to reduce the maximum pad temperature, especially since modern turbomachinery operates at increasingly higher speeds. Reducing pad peak temperature also reduces pad cooling costs. Fig. 19 shows the peak pad and averaged shaft temperatures calculated by CFD. The pocketed TPJB results show reductions in peak pad and averaged shaft temperatures. The power loss reduction and journal lift in the pocketed TPJB lead to a decrease in the temperatures. The journal lift increases the minimum film thickness, and the viscous heating is accordingly lowered.

The static performance of the pocketed TPJB as presented in Figs. 16–19, shows strong benefits. The dynamic performance of the

pocketed TPJB also needs to be demonstrated. The log decrement, as defined by

$$\delta_{dec,i} = \frac{2\pi(real(\lambda_i)/|\lambda_i|)}{\sqrt{1-(real(\lambda_i)/|\lambda_i|)^2}} \ (\lambda_i \ : eigenvalue) \tag{20}$$

is utilized for this purpose below. Log decrements are obtained from the TPJB dynamic coefficients and are frequently employed to estimate the stability of the rotordynamic system with TPJBs [26]. The present study follows the methodology for calculating the dynamic coefficients and log decrement for a Jeffcott rotor supported symmetrically by the two identical TPJBs in Refs. [16–18]. The rotor equilibrium state transitions from stable to unstable as the log dec value changes from positive to negative values. Fig. 20 shows the x and y mode log decrements vs. operating speed and bearing load. The y mode log decrement of the pocketed TPJB is very similar to the smooth TPJB for any speed and applied load condition. Even though the x mode log decrement of the pocketed TPJB is lower than the existing TPJB, the positive stable status is maintained. In this case, there exists a trade-off between drag power loss reduction and stability. The proposed pocketed pad parameters can be varied to balance desired power loss reduction and required log dec.

Fig. 21(b) shows that for the 3 pocketed pad TPJB, the aforementioned static performance changes (benefits) are a function of the smooth TPJB eccentricity ratio. This shows that TPJBs operating at eccentricities lower than 0.5 will experience the greatest benefits in terms of power loss and peak pad temperature reductions, by installing step and pocket modifications. In contrast greater reduction in oil flow rate is improved at higher TPJB eccentricities.

A study was also conducted to determine the static and dynamic performance benefits obtained with only a single pad (2) with a step and pocket. Fig. 21(a) shows that even though the pocket and step are installed only on pad 2, its benefits are clear with power loss reductions ($-2.3\% \sim -10.0\%$). Fig. 22 shows that, unlike the 3 modified pad case, both x and y log decrements remain nearly unchanged relative to the smooth pad case. Note that log decrements correspond to a 5000 N bearing load, since the power loss reduction is negligible when the applied loads are 10,000 N and 15,000 N.

This demonstrates that static performance improvements can be obtained without the loss of load capacity, while maintaining stability. The pocketed TPJB for pad2 only, has shown a better dynamic performance than the pocketed TPJB for all upper pads, in Fig. 22.

The proposed pocketed TPJB is beneficial for TPJB with a pad centrally located opposite to the static load direction. The selection of a 5 pad bearing was intentionally made to demonstrate potential benefits validated by the 3D CFD model results. Similar benefits should result for pocketed TPJBs with fewer or more pads than 5, if there is a centrally located pad opposite the load direction. Pad pockets could be used as a retrofit or in original equipment, to reduce power loss and required oil flowrate.

Fluid film bearings with static loading generally experience cavitation without erosion damage. Cavitation erosion occurs in journal bearing subjected to high dynamic (cyclic) loading, such as may occur during the crank cycle in internal combustion engines [22,23]. Quick, large changes in pressure cause sudden bubble collapse with high impact loads on the bearing surface, leading to erosion pitting. The erosion damage may be reduced with the use of harder material, avoiding severe operating conditions, etc. The proposed bearing is not subject to severely fluctuating load conditions. Thus, it is expected that erosion damage is unlikely, but due to the novel design will be investigated in future work.

5. Conclusion

This study presented a model and simulation study for a modified TPJB for reducing power loss without significant load capacity and/or stability degradation. The proposed TPJB modifies a smooth pad by adding a pocket and a step, on the upper pads which carry relatively low loads, to inhibit load capacity loss. The principal mechanisms involved include (a) lowering the power loss by inducing cavitation inside the pockets, and (b) stabilizing the pad by generating moment balancing pressure peaks at the pocket and step trailing edges. Cavitation generated inside the pockets lowers the dynamic viscosity and the radial component of the circumferential velocity gradient is reduced due to the larger clearance in the pocket. Both effects combine to lower the shear stress that opposes the journal rotation, in effect lowering drag torque. A previously validated, high-fidelity TEHD-CFD model was employed to test the efficacy of an example, 3 modified pad TPJB. The drag power loss reduction was ($-2.4 \sim -27.3\%$) and eccentricity ratio reduction was ($-2.4\% \sim -52.8\%$) for the static TPJB performance. Related benefits include supply oil flow rate reduction ($-2.0 \sim -15.0\%$) and pad peak temperature reduction ($+0.9\% \sim -9.09\%$), gained for various operating speed and applied load conditions.

Computed log decrements for a Jeffcott rotor model supported by 2 identical TPJB, with 3 modified upper pads, showed a decrease in stability margin for the x mode log dec, and near invariance for the y mode log dec, as compared with the smooth pad case. The x log dec remained above +0.9 for the entire speed range, in spite of its reduction relative to the smooth pad case. A second modified bearing model with only 1 modified pad (pad 2) yielded results showing near invariance of both x and y log decrements between the smooth and pocketed TPJB. The power loss reduction for the single pocketed bearing was substantial but less than for the 3 pocketed pad TPJB. These results imply that, as in most engineering design problems, there is a tradeoff between competing objectives, here identified as reducing power loss and increasing rotordynamic stability.

Future work includes experimentally verifying the predictions presented. The example bearing utilized in this study has the dimensions and properties of the bearing in a test rig for measuring bearing power loss at the Texas A&M. The rig is scheduled for completion in 2021. Future work also includes developing machined learning based selection rules and guidelines for pocket and step dimensions and locations. These will be presented with Pareto fronts illustrating tradeoffs between the competing objectives of power loss reduction and log dec maximization.

Declaration of competing interest

The authors declare that they have no known competing financial interests or personal relationships that could have appeared to influence the work reported in this paper.

Acknowledgment

The authors appreciatively acknowledge the funding for this research from the Texas A&M Turbomachinery Research Consortium (TRC) and the Texas A&M High-Performance Research Computing Center (HPRC).

APPENDIX. MODEL VALIDATION

The TEHD-CFD modeling method in Sec. 3 was developed in previous studies [16–18] with geometric parameterizations, and validated against test data. TEHD-CFD TPJB results are correlated with test data here, vs. load and speed. As shown in Table 2, TEHD-CFD simulation results and test data are compared for eccentricity ratio, upper pad temperature (Pad1), bottom pad temperature (Pad4), and supply oil flow rate. The pad temperature

comparisons give important validity information because the pad temperature reflects thermal flow effects, balanced by viscous heating proportional to the power loss, advection heat flows, and heat transfers in the fluid-film domain. Also, the correlation for the eccentricity ratio checks the validity of the TEHD-CFD model. Table 2 shows that the relative errors between the prediction and measurement are mostly within 15% in the various operating conditions, which supports the validity of the TEHD-CFD model.

Table 2
TEHD-CFD Model Validation for a TPJB (50.8 mm Radius, 60.3 mm Length) [18].

Load [N] / Speed [kRPM]	Operating Conditions							
	6337				10,559			
	7	10	13	16	7	10	13	16
Relative Error [%] between CFD and Experiment								
Eccentricity Ratio	13	15	15	2	12	13	12	1
Pad1 Temperature	7	8	5	2	8	9	6	4
Pad4 Temperature	9	2	1	0	10	2	1	5
Supply Oil Flow Rate	14	13	15	15	14	14	15	15

The TEHD-CFD model validation was previously performed when the cavitation is negligible in the fluid-film. Cavitation is especially important inside the pockets of the novel, low loss TPJB, and so a dedicated validation of the cavitation model (Rayleigh-Plesset) was conducted. A dedicated test rig for the proposed low loss bearing is presently unavailable. Therefore, available test data [25] with a similar flow regime (laminar) and conditions with the pocket's saturated cavitation, is utilized to indirectly validate the cavitation model employed in the proposed TPJB CFD study.

Fig. 23 represents the venturi geometry and cavitation features [25] introduced to validate the pocket cavitation model. The pressure measurement points are located at A and B in Fig. 23. The pressure decreases right after the venturi neck, where the cross-section area (y-z plane) starts to increase. The pressure drop near the neck induces the saturated cavitation (oil mist), as depicted in Fig. 23. Gaseous cavitation (air bubbles) also occurs downstream of the neck as shown in Fig. 23. Mineral oils contain mostly 8–12% (by volume) dissolved air [24]. The proposed bearing's CFD simulation results will show that the amount of gaseous cavitation is negligible when compared to the saturated cavitation inside the pockets. The additional consideration of the gaseous cavitation effect does not significantly affect the prediction accuracy for the proposed TPJB, and the consideration is computationally inefficient. Thus, gaseous cavitation is not modeled and is considered a minor consideration in the comparison validation.

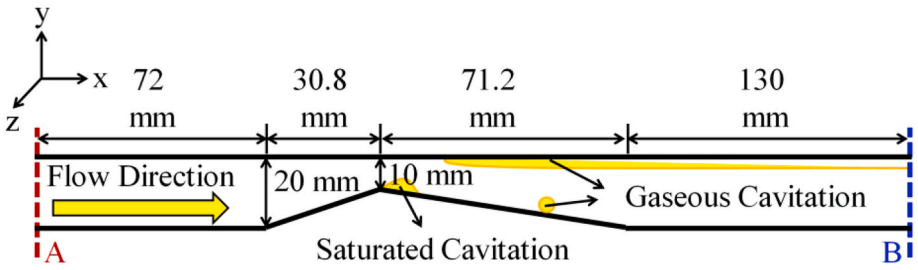

Fig. 23. Venturi Geometry and Cavitation Phenomena in Laminar Flow Regime (Depth: 10 mm) [25]

Table 3
Fluid Property (47V 100 Silicon Oil [25])

Oil Properties	Values
Oil Density [kg/m3]	963
Oil Dynamic Viscosity [Pas]	0.0975
Surface Tension Coefficient [N/m]	0.0209
Saturation Pressure [Pag]	0

Table 3 provides the oil properties applied in the test [25] and CFD simulation. The generated mesh and boundary conditions are illustrated in Fig. 24(a). The mesh density is determined through grid testing, and a denser mesh is made near the wall and venturi neck, as seen in Fig. 24(b). The computational domain is extended in both positive and negative x directions to guarantee fully developed flow conditions from A and to prevent reverse flow at B. The Inlet is prescribed with velocity, and pressure is imposed at the outlet. The loss coefficient per unit length is prescribed in the sub-domains from C to the pressure outlet, to adjust the pressure at A and investigate the cavitation number, that indicates the cavitation inception. The cavitation number (σ) is defined as

$$\sigma = \frac{2(p_A - p_v)}{\rho_f u_A^2} \tag{21}$$

where p_A and u_A are the pressure and velocity at A, and p_v is the saturation pressure 1.3 Pa. CFD simulations considering laminar, isothermal, and mixture multiphase flows with the Rayleigh-Plesset cavitation model were conducted to confirm the selected cavitation model's reliability.

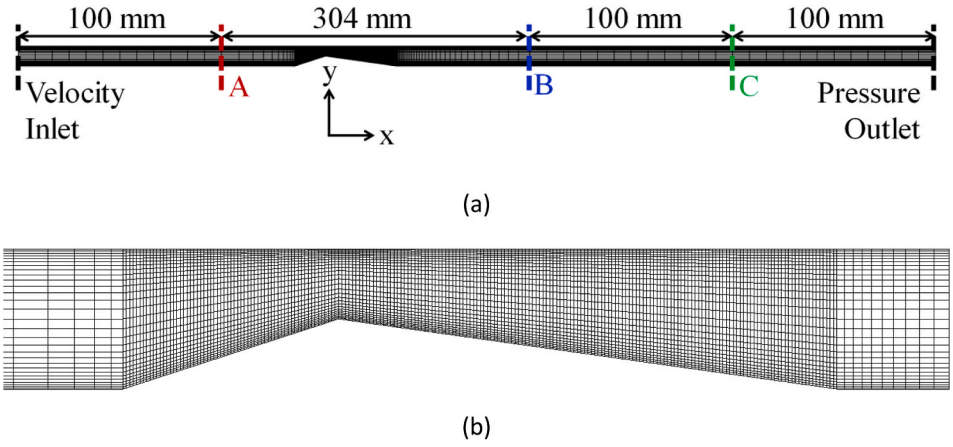

Fig. 24. Mesh with 159,040 Elements for Venturi; (a) Overview, (b) Magnified View near Venturi Neck

Fig. 25 shows the correlations between CFD simulation and experiment for the low Reynolds number range (laminar).

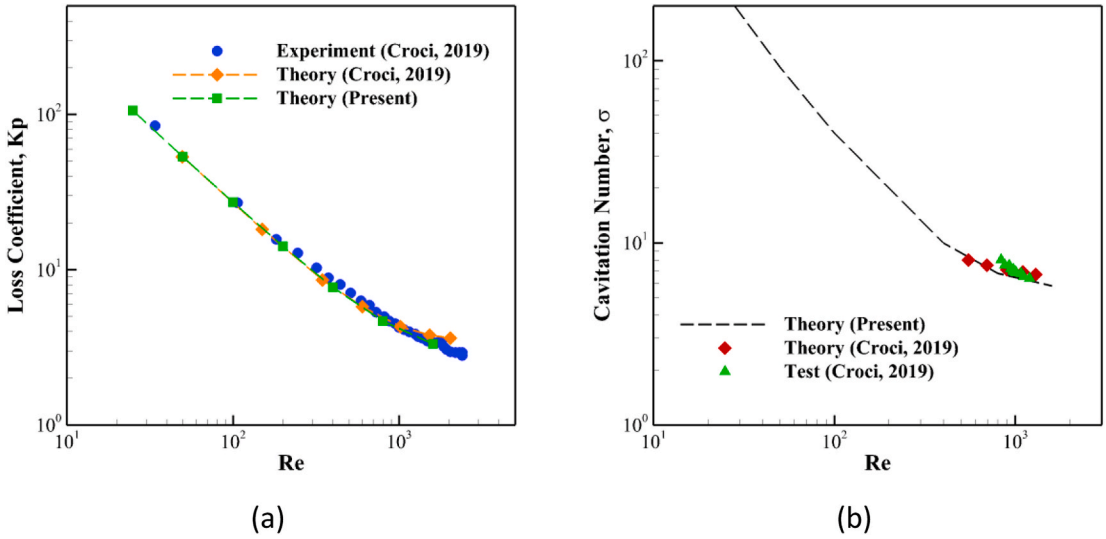

Fig. 25. Comparison between Theory and Experiment [25]; (a) Loss Coefficient (K_p), (b) Cavitation Number (σ)

The pressure loss coefficient is defined as

$$K_p = \frac{2(p_A - p_B)}{\rho_f u_A^2} \tag{22}$$

where p_B is the pressure at B. The CFD simulations agree well with the test data [25] for the pressure loss coefficients represented in Fig. 25(a). The cavitation number in Eq. (21) is calculated from p_A and u_A when the minimum pressure of the domain becomes lower than the saturation pressure, and corresponds to cavitation inception conditions. Fig. 25(b) shows that the CFD simulation accurately predicts the cavitation inception as compared with experimental data. Croci et al. [25] measured the cavity when the Reynolds number is 1201, and the cavitation number is 6.04. The cavity size and location are compared in Fig. 26, and the comparison shows good agreement between the CFD simulated cavity and the test measured cavity. The cavity geometry information in the CFD simulation is identified as where the iso-surface volume fraction is 0.015. The reliability of the mixture multiphase flow and the Rayleigh-Plesset models employed in the full TPJB CFD model, were validated through comparisons between the CFD results and test measurements.

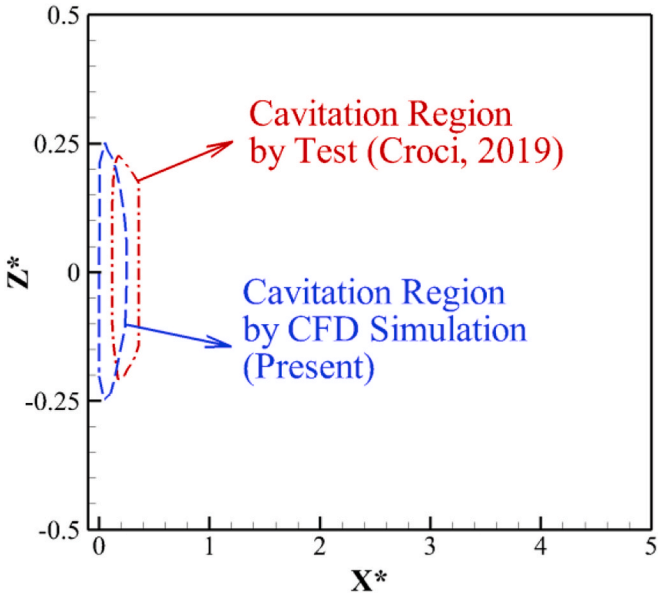

Fig. 26. Cavity Comparison between 3D CFD Simulation and Test [25] (Reynolds Number = 1201, Cavitation Number = 6.04, Nondimensionalized X* and Y* by 10 mm depth; view from above)

References

[1] Holmberg K, Erdemir A. Influence of tribology on global energy consumption, costs and emissions. Friction 2017;5(3):263–84.
[2] Vladescu SC, Fowell M, Mattsson L, Reddyhoff T. "The effects of laser surface texture applied to internal combustion engine journal bearing shells – an experimental study. Tribol Int 2019;134:317–27.
[3] Galda L, Sep J, Olszewski A, Zochowski T. Experimental investigation into surface texture effect on journal bearings performance. Tribol Int 2019;136:372–84.
[4] Khatri CB, Sharma SC. Analysis of textured multi-lobe non-recessed hybrid journal bearings with various restrictors. Int J Mech Sci 2018;145:258–86.
[5] Meng FM, Zhang L, Long T. Effect of groove textures on the performances of gaseous bubble in the lubricant of journal bearing. ASME J Tribol 2017;139(3). 031701.
[6] Shinde AB, Pawar PM. Multi-objective optimization of surface textured journal bearing by Taguchi based Grey relational analysis. Tribol Int 2017;114:349–57.
[7] Meng F, Yu H, Gui C, Chen L. "Experimental study of compound texture effect on acoustic performance for lubricated textured surfaces. Tribol Int 2019;133:47–54.
[8] Yamada H, Taura H, Kaneko S. Static characteristics of journal bearings with square dimples. ASME J Tribol 2017;139(5). 051703.
[9] Nichols BR, Fittro RL, Goyne CP. Steady-state tilting-pad bearing performance under reduced oil supply flow rates. ASME J Tribol 2018;1405. 0151701.
[10] Ding A, Ren X, Li X, Gu C. Friction power analysis and improvement for a tilting-pad journal bearing considering air entrainment. Appl Therm Eng 2018;145:763–71.
[11] Yang S, Kim C, Lee Y. Experimental study on the characteristics of pad fluttering in a tilting pad journal bearing. Tribol Int 2006;39(7):686–94.
[12] Yang S, Kim C, Lee W. Prevention of fluttering fatigue damage in a tilting pad journal bearing. Tribol Int 2009;42(6):816–22.
[13] Bang K, Kim J, Cho Y. Comparison of power loss and pad temperature for leading edge groove tilting pad journal bearings and conventional tilting pad journal bearings. Tribol Int 2010;43(8):1287–93.
[14] Kim J, Palazzolo A. Dynamic characteristics of TEHD tilt pad journal bearing simulation including multiple mode pad flexibility model. ASME J Tribol 1995;117(1):123–35.
[15] Monmousseau P, Fillon M, Frene J. "Transient thermoelastohydrodynamic study of tilting-pad journal bearings—comparison between experimental data and theoretical results. ASME J Tribol 1997;119(3):401–7.
[16] Yang J, Palazzolo A. 3D thermo-elasto-hydrodynamic CFD model of a tilting pad journal bearing-Part I:static response. ASME J Tribol 2019;141(6). 061702.
[17] Yang J, Palazzolo A. 3D thermo-elasto-hydrodynamic CFD model of a tilting pad journal bearing-Part II:dynamic response. ASME J Tribol 2019;141(6). 061703.
[18] Yang J, Palazzolo A. "Computational fluid dynamics based mixing prediction for tilt pad journal bearing TEHD modeling—Part I: TEHD-CFD model validation and improvements. ASME J Tribol 2020;143(1). 011801.
[19] Menter FR. Two-equation eddy-viscosity turbulence models for engineering applications. AIAA J 1994;32(8):1598–605.
[20] Zwart PJ, Gerber AG, Belamri T. A two-phase flow model for predicting cavitation dynamics. In: Proceedings of international conference on MultiphaseFlow, Yokohama, Japan; 2004.
[21] Yin S, Gu C, Ren X. Development and validation of a gaseous cavitation model for hydrodynamic lubrication. Proc IMechE Part J J Eng Tribol 2015;229(10):1227–38.
[22] Garner DR, James RD, Warriner JF. Cavitation erosion damage in engine bearings: theory and practice. J Eng Gas Turbines Power 1980;102(4):847–57.
[23] Dowson D, Taylor CM. Cavitation in bearings,. Annu Rev Fluid Mech 1979:35–66.
[24] Pinkus O. Thermal aspects of fluid film tribology. New York: ASME Press; 1990. p. 187–97.
[25] Croci K, Ravelet F, Danlos A, Robinet JC, Barast L. Attached cavitation in laminar separations within a transition to unsteadiness. Phys Fluids 2019;31(6). 063605.
[26] Oh J, Kim BJ, Palazzolo A. Three-dimensional solid finite element contact model for rotordynamic analysis: experiment and simulation. ASME J Vib Acoust 2021;143(3). 031007.